The X-Linked Intellectual Disability gene, *ZDHHC9*, is important for oligodendrocyte maturation and myelin formation

Authors: Hollman, RB[1]; Wild, AR*[1]; O'Leary, TP*[1]; Thompson, AJ[1]; Flibotte, S[2]; Poblete, TO[1]; Peng, A[1]; Rogalski, JC[3]; Gill, G[1] and Bamji, SX[1]

* These authors contributed equally

Affiliations:

1 Department of Cellular and Physiological Sciences, Life Sciences Institute and Djavad Mowafaghian Centre for Brain Health, University of British Columbia

2 Life Sciences Institute Bioinformatics Facility, University of British Columbia

3 Department of Biochemistry and Molecular Biology, University of British Columbia

Correspondence:
Shernaz Bamji, Ph.D.
Department of Cellular and Physiological Sciences
Life Sciences Institute,
Djavad Mowafaghian Centre for Brain Health
University of British Columbia
2350 Health Sciences Mall
Vancouver, B.C., V6T 1Z3
Off: 604-822-4746

Acknowledgements:
We thank the UBC Proteomic Core as well as Naoji Yubuki and the UBC Bioimaging Facility (RRID: SCR_021304) and the UBC School of Biomedical Engineering Sequencing Core at the Biomedical Research Center for technical help. Dr. Mark Cembrowski's lab (UBC) provided expertise on FISH. This work is supported by grants from CIHR (FDN-159907) (S.X.B.) and NIH (AWD-020422) (G.T., S.H.K., & S.X.B.), as well as by computational resources made available through the NeuroImaging and NeuroComputation Centre at the Djavad Mowafaghian Centre for Brain Health (RRID:SCR_019086) and the Dynamic Brain Circuits in Health and Disease Research Excellence Cluster DataBinge Forum.

Declaration of Interest:
The authors declare no competing interests.

Keywords:
Palmitoylation, ZDHHC9, oligodendrocytes, corpus callosum, differentiation, myelination, mouse model, X-linked intellectual disability,

SUMMARY

Two percent of all patients with X-linked intellectual disability (XLID) exhibit loss-of-function mutations in the palmitoylating enzyme, *ZDHHC9*[1,2]. One of the main anatomical deficits observed in these patients is a decrease in corpus callosum volume and a disruption of white matter integrity[3–6]. We demonstrated that ablation of *Zdhhc9* in mice substantially impairs the maturation of oligodendrocytes, resulting in fewer mature, myelinating oligodendrocytes, higher numbers of oligodendrocyte progenitor cells and a decrease in the density of myelinated axons. Ultrastructural analysis of the remaining myelinated axons in the corpus callosum revealed further disruptions in myelin integrity. RNA sequencing and proteomic analyses revealed a concomitant decrease in the expression of genes and proteins involved in lipid metabolism, cholesterol synthesis and myelin compaction. These results reveal a previously underappreciated and fundamental role for ZDHHC9 and protein palmitoylation in regulating oligodendrocyte differentiation and myelinogenesis and provide mechanistic insights into the deficits observed in white matter volume in patients with mutations in *ZDHHC9*.

INTRODUCTION

ZDHHC9 is one of a family of 23 palmitoyl acyl transferases that catalyze *S*-acylation, the reversible addition of acyl groups onto proteins through a labile thioester bond[7]. In the brain, palmitoylation is the most common form of *S*-acylation and directly influences protein trafficking, function, and stability[7]. Loss-of-function (LOF) mutations in the *ZDHHC9* gene (which is located on the X-chromosome) have been reported in ~2 % of male patients diagnosed with X-linked intellectual disability (XLID)[1,2,4–6,8–10], with ~75% of these patients exhibiting epileptic comorbidities[3]. Deletion of *Zdhhc9* in mice (Gene nomenclature: "*ZDHHC9"* in humans and "*Zdhhc9"* in mice) results in cognitive deficits that mirror those observed in human patients[11]. Our lab has shown that ablating *Zdhhc9* can profoundly reduce dendritic branching, disrupt the formation of inhibitory synapses and increase seizure-like activity[12]. Magnetic Resonance Imaging (MRI) on patients[3–6] and mice[11] lacking ZDHHC9 demonstrate a striking decrease in the volume of the corpus callosum, a large white matter tract that connects the two hemispheres of the brain[13]. In accordance with this, single-cell RNAseq studies reveal that *Zdhhc9* is most highly expressed in the corpus callosum and in myelinating oligodendrocytes[14]. Notably, *Zdhhc9* is the most highly expressed palmitoylating enzyme in oligodendrocytes at postnatal day 23[15]—the period of peak myelination of the corpus callosum[16]. Despite the fact that ZDHHC9 is highly expressed in the corpus

callosum and that the volume of the corpus callosum is significantly attenuated in patients and mice lacking ZDHHC9, the role of ZDHHC9 in white matter development remains unexplored.

Here we systematically examined the role of Zdhhc9 in the corpus callosum using RNAseq to determine which genes are differentially expressed in *Zdhhc9* knockout mice compared to control, and proteomics to identify proteins that are differentially expressed specifically in purified myelin. This data, together with electron microscopy (EM) and fluorescent in situ hybridization (FISH) demonstrate that *Zdhhc9* is important for the differentiation of oligodendrocyte precursor cells to mature oligodendrocytes resulting in fewer mature oligodendrocytes and fewer myelinated axons in *Zdhhc9* knockout mice. We also show that *Zdhhc9* is important for myelin integrity and that ablation of *Zdhhc9* results in disruptions in myelin compaction. Our work provides a mechanistic understanding of the role of ZDHHC9 in white matter and provides an explanation for the decrease in white matter volume in patients with *ZDHHC9* mutations and a plausible explanation for epileptic comorbidities and intellectual disability.

RESULTS AND DISCUSSION:

Axonal organization in the corpus callosum is heterogenous and organized in a spatially segregated manner according to projection neuron origin and corresponding targets in the contralateral hemisphere[17] (Figure S1A). Despite this heterogeneity, we observed a robust and relatively homogenous reduction in the width of the corpus callosum, hippocampal commissure and external capsule in postnatal day 60 (P60) *Zdhhc9*-KO male mice at all regions analyzed along the antero-posterior axis (Figure S1A-F) as well as a relatively homogenous expression of *Zdhhc9* along the anterior-posterior axis (Figure S1G,H). To date, only male patients have been identified to have XLID with *ZDHHC9* loss of function mutations, and accordingly only male mice were used in this study.

Zdhhc9 deletion decreases mature oligodendrocyte marker gene expression in the corpus callosum and optic nerve

To investigate why the corpus callosum size is reduced in *Zdhhc9*-KO mice, we performed bulk RNAseq on the microdissected corpus callosum of control and *Zdhhc9*-KO mice (Figure 1A). We identified 173 differentially expressed genes (Table S1 for RNAseq raw data; Table S2 for the list of 173 differentially expressed genes organized by gene ontology {GO} annotation). Of the differentially expressed genes, 52 were upregulated and 121 genes were downregulated in *Zdhhc9*-KO mice (Figure 1B). Aside from *Zdhhc9* itself, there was no significant change in the expression of other ZDHHC enzymes or palmitoyl thioesterases (enzymes that catalyze the removal of palmitate), suggesting no compensatory changes in other enzymes that regulate palmitoylation (Table S1). Notably, of all the ZDHHC enzymes, *Zdhhc9* was

the most highly expressed ZDHHC enzyme in the corpus callosum of control P60 male mice, in line with previous studies[14,18] (Table S1).

To investigate which cell types in the corpus callosum were most affected by loss of *Zdhhc9,* we identified marker genes that were differentially expressed in *Zdhhc9*-KO mice. Marker genes are defined as a set of genes with highly enriched expression in a particular cell type, and changes in their expression can be used to estimate changes in cell type proportions in bulk RNAseq data[14,19–21]. Of our 173 differentially expressed genes, we identified 13 downregulated genes that are markers for mature oligodendrocytes (MOLs), microglia, and astrocytes (Figure 1B). Within our upregulated genes, we identified only one marker gene, which corresponded to excitatory neurons. These results reveal substantial changes in gene expression and a potential decrease in the number of mature oligodendrocytes in the corpus callosum of *Zdhhc9*-KO mice.

Oligodendrocyte differentiation is a stepwise process which can be separated into three main stages: (I) the precursor stage, (II) the immature pre-myelinating stage, and (III) the mature myelinating stage[22]. Corresponding to these stages are four oligodendrocyte subtypes: OPC (stage I), newly formed oligodendrocyte (NFOL) and myelin forming oligodendrocytes (MFOL; stage II), and MOL (stage III)[15].

To further investigate which oligodendrocyte subtypes might be impacted by loss of *Zdhhc9*, we leveraged previously published single-cell RNAseq expression data to examine the expression of our differentially expressed genes across oligodendrocyte subtypes[23]. Gene Expression Z-scores were plotted for each oligodendrocyte subtype, with a high Z-score indicating enrichment within a particular cell type. We found that most genes that were up-regulated in *Zdhhc9*-KO mice were enriched in OPCs, while most down-regulated genes were enriched in MOLs, again indicating changes in overall cell type proportions, potentially due to disruption in the maturation of oligodendrocytes (Figure 1C).

To determine potential mechanisms and pathways that are perturbed by *Zdhhc9* ablation we completed PANTHER gene ontology (GO) enrichment analysis for biological processes on the differentially expressed genes. An analysis of downregulated genes revealed enrichment in numerous processes related to cholesterol and sterol metabolism and biosynthesis, whereas upregulated genes were enriched in pathways with the broad designation “signaling” (Figure 1D). Downregulated genes had a larger fold change compared to upregulated genes and smaller FDR values, indicating stronger enrichments in biological processes for downregulated genes.

We next examined the relationships between our 173 genes of interest using STRING (Search Tool for the Retrieval of Interacting Genes) protein-protein interaction network analysis (Figure S2). We identified two main clusters of genes related to the immune system (highlighted in green) and cholesterol metabolism (highlighted in orange). The immune cluster included genes associated with microglia (such as *Ctss*, *C1qa*, *Ly86*, *Laptm5*, *Csf1r*; Figure 1B and Figure S2). Most genes in these clusters were downregulated, suggesting a potential impairment in both immune regulation and cholesterol metabolism in *Zdhhc9*-KO mice.

We next performed quantitative reverse transcriptase polymerase chain reaction (qRT-PCR) on six selected genes that were identified in key signaling networks in our RNAseq analysis, including myelin formation (*Mobp*), myelin assembly (*Pmp22*), glial cell differentiation (*Hapln2*), lipid transport (*Apod*, *Slco3a1*) and lipid metabolism (*Ldlr*). We confirmed decreased expression of all six of these genes in line with our RNAseq data and supporting the robustness of our dataset (Figure 1E).

Previous studies have identified several ZDHHC enzymes that can modulate gene expression through the palmitoylation of transcription factors[26–29], chromatin remodelers[30–32], and histones[33,34]. Thus, altered gene expression observed in the corpus callosum of *Zdhhc9*-KO mice could be a result of changes in the palmitoylation of these substrates as well as signaling pathways that alter gene transcription. Notably, in our dataset we identified altered expression of several genes encoding proteins that further regulate gene expression. For example, we observed decreased expression of *Insig1*, a modulator of sterol regulatory element-binding proteins (SREBPs)[35], which are key regulatory transcription factors for lipid metabolism and synthesis[36]. The decreased expression we observed in a large cluster of genes involved in cholesterol metabolism is particularly interesting, given that cholesterol is the only essential lipid in myelin membranes[37] and is known to regulate the extent of myelination[38,39], influence myelin compaction[40], and acts as a signaling molecule to drive oligodendrocyte differentiation and maturation[41].

We also performed RNAseq on two additional micro dissected brain regions, including the primary visual cortex, in which seizure activity is present in *Zdhhc9*-KO mice[12], and the optic nerve, another large white matter tract. Although we did not identify any differentially expressed genes in the visual cortex, we identified 21 significantly downregulated and 14 significantly upregulated genes in the optic nerve of *Zdhhc9*-KO animals (Figure 3A; Table S3). Similar to the corpus callosum, marker gene analysis highlighted a downregulation of MOL marker genes. In the optic nerve we also observed an upregulation of MFOL marker genes (Figure 3A; Table S3). Analysis of gene expression across

oligodendrocyte subtypes demonstrated that upregulated genes were enriched in MFOLs and downregulated genes were enriched in MOLs (Figure 3B; Table S3), further pointing to disruption of MOLs in the optic nerve. 5 genes were significantly downregulated in both corpus callosum and optic nerve, including *Apln*, *Selenop*, *Slc45a3*, *Pmp22*, and *S100b*, several of which play a role in oligodendrocyte differentiation and/or myelination[42–45]. The shared decreases in gene expression observed in both the corpus callosum and optic nerve suggest broader changes occur in white matter gene expression due to *Zdhhc9* loss, as well as more specific alterations in individual regions.

Zdhhc9 deletion disrupts the maturation of oligodendrocytes in the corpus callosum

Together, changes in gene expression predict a disruption in the maturation of oligodendrocytes in *Zdhhc9*-KO mice. We therefore set out to directly quantify the density of each oligodendrocyte subpopulation in control and *Zdhhc9*-KO mice using fluorescent *in situ* hybridization (FISH). Probes for oligodendrocyte lineage cells were generated, guided by expression data from previously published single-cell RNAseq and FISH studies[15,23]. We chose marker genes with highly enriched expression in their respective target cell types in the brain, including *Pdgfra* (OPC marker), *Itpr2* (NFOL marker), *Ctps* (MFOL marker) and *Hapln2* (MOL marker; Figure S4A). Importantly, we found no difference in the mean expression of each marker gene per cell for control vs *Zdhhc9*-KO mice within their target cell type, confirming that these genes are valid marker genes in both genotypes, and their expression can be used to infer changes in cell number (Figure S4B). Although we found no changes in the overall density of oligodendrocyte lineage cells in P60 adult male mice (Figure 2A-C), we saw a significant increase in the density of OPCs with a concurrent decrease in the density of MOLs in *Zdhhc9*-KO mice (Figure 2A, B, D), and no changes in the density of intermediate maturity oligodendrocyte lineage cells. These results are consistent with our RNAseq results indicating changes in the cell type proportions of oligodendrocyte lineage cells of the corpus callosum in *Zdhhc9*-KO mice, and provide evidence that *Zdhhc9* is important for oligodendrocyte maturation from OPC to MOL.

Zdhhc9 deletion results in fewer myelinated axons and myelin compaction abnormalities

We next did ultrastructural analyses of the corpus callosum using Transmission Electron Microscopy (TEM) on sagittal brain sections of P60-100 male mice. While we observed no difference in total axon density (myelinated and unmyelinated axons) (Figure 3A,B), there was a significant reduction in the number of axons that were myelinated in *Zdhhc9* KO mice (Figure 3A,C). This was consistent with an observed decrease in the density of nodes of Ranvier (Figure S6). We also quantified an increase in the diameter of myelinated axons in *Zdhhc9* KO mice (Figure 3A,D), and an increase in average g-ratio

corresponding with the hypomyelination of axons (Figure 3E,F). Analysis of the ultrastructure of myelinated axons demonstrated a significant increase in the number of axons with myelin abnormalities (Figure 3G, arrowheads in 3A) which often resembled residual myelin loops observed in other conditional knock-out mice with disruptions in myelin compaction[46] . To test this further, we measured the distance between intraperiod and major dense lines and demonstrated an increase in this distance (increased periodicity) in *Zdhhc9*-KO mice further demonstrating deficits in myelin compaction (Figure 3H). This result could in part be explained by a downregulation of genes we identified in the corpus callosum such as *Apod* and *Pmp22* (Figure 1B,C), which are known to regulate myelin compaction[47,48]. Interestingly, residual myelin loops and uncompacted myelin are typically observed in immature myelin[49,50], consistent with our FISH data showing fewer mature oligodendrocytes in *Zdhhc9*-KO mice. Similar ultrastructural white matter deficits are observed in both human patients with epilepsy[51,52] and rat models of epileptic seizures[53,54], supporting the idea that dysmyelination might influence seizure activity in *Zdhhc9*-KO mice.

Zdhhc9 deletion decreases the expression of integral myelin proteins in the myelin proteome

To better understand how ablation of *Zdhhc9* can impact myelin integrity and compaction in, we looked for changes in the myelin proteome using mass spectrometry. We isolated myelin from the whole brain of P23 male mice, an age corresponding with peak myelinogenesis[16] and peak expression of *Zdhhc9*[14] (Figure 4A). Whole brains were used as patients with XLID and *ZDHHC9* LOF mutations exhibit white matter reductions throughout the brain including the corpus callosum, temporal lobes, optic nerve and pituitary stalk[3]. We identified 1930 proteins in at least 3 of 4 wildtype samples (Table S4, Figure S6A), and 1987 proteins in at least 3 of 4 *Zdhhc9*-KO samples (Table S4, Figure S6b). Of these, 1864 proteins were identified in both genotypes (Table S4, Figure S6C). We observed significant differences in the myelin proteome, with 84 proteins upregulated and 113 proteins downregulated in *Zdhhc9*-KO mice (Figure 4B). Note that ZDHHC9 is not listed as differentially expressed because it was not detected in any *Zdhhc9*-KO samples. Of the top 15 most abundantly expressed myelin proteins, 4 were significantly downregulated in *Zdhhc9*-KO mice (Figure 4C). This included proteins that regulate myelin compaction (CLDN11, MOBP, SIRT2)[55–58], and one protein that has been shown to regulate oligodendrocyte differentiation and the maintenance of mature myelin (MAG)[59]. GO term annotation of the 197 differentially expressed proteins showed an association with 25 different biological processes including axon ensheathment, lipid binding, and lipid metabolism (Table S5, Figure 4D).

Interestingly, ZDHHC9 was the only palmitoyl acyl transferase detected in isolated myelin, suggesting a crucial role for this enzyme in regulating the dynamic palmitoylation of myelin proteins within the myelin sheath. Four depalmitoylating enzymes in the ABHD family of palmitoyl thioesterases were identified in control myelin and of these, two (ABHD4 and ABHD17B) were significantly reduced in *Zdhhc9*-KO mice (Figure 4E). Changes in the myelin proteome of *Zdhhc9*-KO mice could be due to altered gene expression, protein stability and/or disrupted targeting and sorting of protein into the myelin membrane. Indeed, palmitoylation has been shown to be required for trafficking key myelin proteins into the myelin sheath[60] and previous work from our lab has identified key myelin proteins including MOBP and PLP to be substrates for ZDHHC9[14]. Overall, the findings of this study establish a critical role for ZDHHC9 in oligodendrocyte development and myelination and identify numerous dysregulated signaling pathways that may underlie the decrease in white matter volume, epileptic comorbidities and intellectual disability seen in patients with *ZDHHC9* mutations.

FIGURE CAPTIONS:

Figure 1: There is a decrease in MOL marker gene expression and genes involved in lipid metabolism in the corpus callosum of *Zdhhc9*-KO mice. a, Illustration showing the region sampled for RNAseq analysis. **b,** Quantification of fold change in gene expression (*n* = 5 *Zdhhc9*-KO, *n* = 6 control). Each point represents an individual gene; blue denotes genes that are downregulated, and red denotes genes that are upregulated in *Zdhhc9*-KO mice relative to controls. The horizontal line denotes the statistical significance threshold required for two tailed t-tests; p-values were adjusted to account for multiple comparisons. Differentially expressed cell type marker genes are labelled. **c,** Heatmaps showing the expression of the 173 differentially expressed genes within different oligodendrocyte subtypes using single cell RNAseq data from Mousebrain. Genes are listed (top to bottom) by decreasing $\log_2$ Fold Change (i.e. from most to least upregulated and least to most downregulated). Dotted black boxes highlight overall enrichment of upregulated and downregulated genes. **d,** Enrichment analysis for Biological Process GO terms for both up- and downregulated genes. The ten GO terms with largest fold enrichment based on FDR value are shown. **e,** Graph of RT-qPCR data for a subset of differentially expressed genes with known roles in myelination (*n* = 4-6 *Zdhhc9*-KO, control). Normalized expression of each gene relative to control (dotted line).

Figure 2: There is a decrease in the density of MOLs and an increase in the density of OPCs in the corpus callosum of *Zdhhc9*-KO mice. a, Representative images of fluorescent *in situ* hybridization for oligodendrocyte cell-lineage-subtype marker genes (*Pdgfra* -OPCs, *Itpr2* -NFOLs, *Ctps*-MFOLs, *Hapln2* -MOLs) within the corpus callosum (scale bar, 50μm). **b,** Representative images of DAPI cell nuclei masks pseudocolored by oligodendrocyte subtype classification (yellow – OPCs, cyan – NFOLs, magenta – MFOLs, green – MOLs, grey – none). **c,** Density of oligodendrocyte lineage cells (sum of all OPC, NFOL, MFOL and MOL cells) in control and *Zdhhc9*-KO mice (*n* = 4 *Zdhhc9*-KO, *n* = 5 control). **d,** The density of cells within each of the four major oligodendrocyte subtypes in *Zdhhc9*-KO and control mice. Data in **b** and **c** are mean + SEM, unpaired two-tailed Student's t-tests.

Figure 3: There are fewer myelinated axons and increased myelin decompaction in the corpus callosum of *Zdhhc9*-KO mice. a, Representative transmission electron microscopy images of the corpus callosum in *Zdhhc9*-KO and control mice (scale bar, 2μm). **b,** The density of axons and **c,** the percentage of axons that are myelinated in *Zdhhc9*-KO and control mice (*n* = 3 mice per genotype). **d,** Frequency distribution graph showing the diameter of myelinated axons in the corpus callosum. **e,** The average g-

ratio of myelinated axons (*n* > 1000 axons from 3 separate control and *Zdhhc9*-KO mice). **f,** Frequency distribution graph showing the proportion of myelinated axons with a given g-ratio. **g,** Representative images (left) and quantification (right) of axons with myelination decompaction phenotypes (myelin "loops") (scale bar, 1μm). **h,** Representative images of a myelinated axon, showing major dense line (MDL) and intraperiod line (IL) within the myelin sheath (scale bar, 100nm) (left) and quantification of the average distance between IL and MDL (*n* > 30 axons from 3 separate control and *Zdhhc9*-KO mice). Data in **b, c, e, f, g, h** show mean + SEM. **b, c, g, h,** unpaired two-tailed Student's t-tests; **d, f,** Kolmogorov-Smirnov test; **e,** Welch's t-test

Figure 4: Proteins associated with myelination and myelin compaction are decreased in *Zdhhc9*-KO mice. a, Illustration showing the pipeline for myelin proteomic analysis. **b,** Quantification of fold change in protein expression (*n* = 4 mice per genotype). Each point represents an individual protein; blue denotes proteins that are downregulated, and red denotes proteins that are upregulated in *Zdhhc9*-KO mice relative to controls. The horizontal line denotes the statistical significance threshold required for two tailed t-tests. Labelled proteins denote those that are both differentially expressed and highly abundant (top 10% of control myelin proteome). **c,** Graph of Max LFQ Intensity data for the 15 most abundant myelin proteins (*n* = 4 mice per genotype). Normalized expression of each protein relative to control (dotted line). Differentially expressed proteins are highlighted in green. **d,** Graph of the biological process GO Term associated with each differentially expressed protein along with their $\log_2$ Fold Change. **e,** Graph of Max LFQ Intensity data for all palmitoylating enzymes identified in myelin (*n* = 4 mice per genotype). All statistical analyses were done using unpaired two-tailed Student's t-tests.

Figure S1: There is a uniform reduction in the width of white matter tracts in *Zdhhc9*-KO mice and a uniform expression of *Zdhhc9* throughout the anterior posterior axis of the corpus callosum. a, (Top left) Schematic of the brain (horizontal plane), illustrating the spatial relationship between the position of cortical regions and the respective location their projections cross the anterior posterior axis of the corpus callosum. (Right) Schematic of the anterior-posterior axis of the corpus callosum, colored based on its main anatomical subdivisions: genu (red), body (blue), splenium (green). The location of these colored regions indicates where measurements were taken for subsequent morphological analyses. **b,** Representative image illustrating white matter tracts that were quantified (corpus callosum, hippocampal commissure, external capsule), and the relative position where measurements were taken within each tract (scale bar, 1mm). **c,** Width of the corpus callosum (*n* = 4 *Zdhhc9*-KO, *n* = 6 control) **d,**

the external capsule and **e,** the hippocampal commissure in control and *Zdhhc9*-KO mice. (*n* = 5 *Zdhhc9*-KO, *n* = 6 control) **f,** Representative images of the posterior location at which the corpus callosum terminates in control and *Zdhhc9*-KO mice (scale bar, 1mm). Distance from bregma at which the corpus callosum terminates in control and *Zdhhc9*-KO mice. **g,** Representative image of FISH for *Zdhhc9* along the anterior-posterior axis of the corpus callosum (scale bar, 1mm). White matter tracts are labeled with dashed lines, along with the main subdivisions of the corpus callosum (colored as in **a,**). **h,** Percent coverage of *Zdhhc9* labeling per cell as a function of distance from the origin of the corpus callosum. Points are colored based on sub-regions delineated in **h,** (*n* of at least 500 cells per region from 1 animal). Data in **c, d, e, f,** represent mean + SEM, all statistical tests were two-tailed unpaired Student's t-tests. CC=corpus callosum, HC=hippocampal commissure, FO=Fornix, VHC=Ventral hippocampal commissure, AC=anterior commissure.

Figure S2: Protein-protein interaction analysis of differentially expressed genes. STRING analysis highlighting protein-protein interactions between differentially expressed genes identified from RNAseq (left). Blue nodes represent downregulated genes, red nodes represent upregulated genes and the node size depicts the magnitude of the fold change in gene expression. Lines (edges) between nodes show predicted protein-protein interactions, and the corresponding line-width reflects the confidence of protein-protein interactions. Two groups of proteins with high densities of interactions were noted and contain proteins with known roles in cholesterol metabolism (orange circle) and immune system function (green circle). Differentially expressed genes without predicted protein-protein interactions are also shown (right).

Figure S3: There is change in gene expression in the optic nerve of *Zdhhc9*-KO mice. **a,** Quantification of fold change in gene expression in *Zdhhc9*-KO optic nerve compared to control mice (*n* = 5 *Zdhhc9*-KO, *n* = 4 control). Each point represents an individual gene; blue denotes genes that are downregulated, and red denotes genes that are upregulated in *Zdhhc9*-KO mice relative to controls. The horizontal line denotes the statistical significance threshold required for two tailed t-tests; p-values were adjusted to account for multiple comparisons. Differentially expressed cell type marker genes are labelled. **b,** Heatmaps showing the expression of the 35 differentially expressed genes within different oligodendrocyte subtypes using single-cell RNAseq data from Mousebrain. Genes are listed (top to bottom) by decreasing $\log_2$ Fold Change (i.e. from most upregulated to the most downregulated). Dotted black boxes highlight overall enrichment of upregulated and downregulated genes.

Figure S4: Overall levels of oligodendrocyte lineage marker gene expression does not differ between *Zdhhc9*-KO and control mice. a, Heatmap of gene expression for our oligodendrocyte lineage marker genes, across different cell types and maturation stages within the oligodendrocyte lineage (single-cell RNAseq from Mousebrain). **b,** Graphs depicting the average coverage of oligodendrocyte lineage probes per cell *(n* = 4 mice per genotype). Data shows mean + SEM, and statistical analyses were done using unpaired two-tailed Student's t-tests.

Figure S5: There is a reduction in the density of nodes of Ranvier in *Zdhhc9*-KO mice. a, Illustration of a myelinated axon and node of Ranvier. **b,** Representative images of the nodal marker, NAV1.6, within the corpus callosum of *Zdhhc9*-KO and control mice (scale bar, 10μm). **c,** The density of nodes and **d,** the length of nodes in *Zdhhc9*-KO and control mice (*n* = 6 *Zdhhc9*-KO, *n* = 7 control). Data in **c,** and **d,** represent mean + SEM, statistical tests were done using unpaired two-tailed Student's t-tests.

Figure S6: Analysis of proteins identified in both *Zdhhc9*-KO and control myelin samples. Venn diagrams showing the overlap of proteins identified in **a,** control and **b,** *Zdhhc9*-KO samples. **c,** Venn diagram of myelin proteins identified in at least 3 *Zdhhc9*-KO and control samples.

METHODS

Animals:

Zdhhc9-KO mice (B6;129S5-Zdhhc9tm1Lex/Mmucd) were originally obtained from the Mutant Mouse Resource and Research Center (MMRRC, University of California Davis). A mutation in *Zdhhc9* was introduced through homologous recombination, targeting coding exon 1 (NCBI ascension: NM_172465.1). All experiments were performed on mice between 2-4 months of age, except for analysis of the myelin proteome, where mice were 23 days of age. Mice were housed in same-sex groups of 2-5 within optimouse cages, with bedding, a plastic hut and nesting material for enrichment. Food and water were available *ad-libitum*. Ear notches were collected at weaning (21 days of age) for identification, and genotyped by Transnetyx (Cordova, TN). All procedures followed guidelines from the Canadian Council on Animal Care and were approved by the UBC Animal Care Committee.

Fluoromyelin staining and analysis:

Thickness and area measurements were obtained using across six regions (each 350-600um in length) spanning the anterior-posterior axis of the corpus callosum. Measurements were obtained from two regions within each of the Genu (**G1**: 1.1-0.74, **G2**: 0.62-0.26), Body (**B1**: -0.01 to -0.58, **B2**: -0.82 to -1.34) and Splenium (**S1**:-1.45 to -1.82, **S2**: -1.94 to -2.54) of the corpus callosum, based on stereotaxic coordinates in Franklin and Paxinos[61]. For each mouse, 2-3 sections were sampled from each region, and measures were obtained either at midline, or averaged bilaterally across cerebral hemispheres.

Tissue collection for RNA-sequencing:

Mice were anesthetized under isoflurane (5%, 1.5L/min), and decapitated. Brains and optic nerves were dissected, and flash frozen in pre-chilled isopentane at -52°C for 30 seconds. Brains were then stored at -80°C until sectioning. The corpus callosum (Bregma 0.98mm – Bregma 0.62mm) was sectioned coronally at 100µm on a cryostat and mounted onto glass slides. Slides were then stored at -80°C until used. Corpus callosum samples were dissected from frozen brain sections, while being cooled on dry ice. RNA was extracted from samples using the Total RNA Purification Micro Kit (Cat. 35300, Norgen Biotek Corp) following the supplied protocol. Samples were then kept at -80°C until analyzed by the RNA sequencing core at the School of Biomedical Engineering Sequencing Core at the Biomedical Research Center (University of British Columbia).

RNA-sequencing:

Sample quality control was performed using the Agilent 2100 Bioanalyzer or the Agilent 4200 Tapestation. Qualifying samples were then prepped following the standard protocol for the Illumina Stranded mRNA prep (Illumina). Sequencing was performed on the Illumina NextSeq2000 with Paired End 59bp × 59bp reads.

RNA-sequencing analysis:

RNA-seq raw sequencing reads were processed with kallisto[62] using the reference transcriptome for mm10 downloaded from Ensembl (www.ensembl.org) and the resulting counts for different isoforms were summed up to obtain counts at the gene level for each sample. The differential expression analysis was then performed with DESeq2[63] and genes achieving the significance cut-off of FDR < 0.05 were considered significantly differentially expressed. Marker genes for each cell type were extracted from the file l5_all.agg.loom downloaded from the Mousebrain website (http://mousebrain.org/adolescent/downloads.html).

Quantitative PCR:

Total RNA was extracted from samples using the Total RNA Purification Micro Kit (Cat. 35300, Norgen Biotek Corp) following the supplied protocol. Quantitative PCR with reverse transcription was performed on a ViiA 7 instrument (Thermo Fisher Scientific) using SYBR Green master mix (Thermo Fisher Scientific). The relative amounts of the messenger RNAs studied were determined by means of the $2^{-\Delta\Delta C}$T method, with Gapdh as the reference gene and the control genotype as the invariant control.

Bioinformatics:

Biological process enrichment analysis was done using PANTHER overrepresentation test (Released 2022-10-13). Functional interaction networks of the differentially expressed genes were investigated using the Search Tool for the Retrieval of Interacting Genes (STRING) 11.5[64]. A threshold confidence level of 0.4 was used to identify protein interactions and seven types of protein interactions were used for network generation, including neighborhood, gene fusion, co-occurrence, co-expression, experimental, database knowledge, and text mining. The Mouse Genome Informatics (RRID:SCR_006460) database[65] was used to assign GO classifications for the list of differentially expressed genes and differentially expressed proteins.

Transcardiac perfusions:

Mice were anesthetized under isoflurane (5%, 1.5L/min), and chest cavity exposed. Transcardiac perfusions were completed with 10ml of PBS (0.1M, pH 7.4) followed by 50ml of 4% PFA in PBS cooled on ice. Brains were removed and post-fixed in 4% PFA overnight. Brains were then cryoprotected in 10% sucrose in PBS for 24 hrs, followed by 30% sucrose for a minimum of 48 hours before sectioning. Mice used for electron microscopy were perfused with 10ml of phosphate buffer solution, followed by 50ml of 2% PFA and 2.5% glutaraldehyde in sodium cacodylate buffer (0.1M, pH 7.4), and post-fixed overnight in the same solution. Mice used for myelin proteomics were perfused with physiological saline buffer, and flash frozen in pre-chilled isopentane.

Cryosectioning:

The entire cerebrum from brains was sectioned coronally at 40µm thickness using a cryostat (Leica 3050S, Leica Microsystems, Wetzlar, Germany). Sections were collected in series of 12, with ~15 sections per series. Sections were placed in anti-freeze cryoprotectant solution for long-term storage at -20°C. For FISH, brains were sectioned at 20µm at regions containing the genu and splenium of the corpus callosum, and sections were mounted onto glass slides. Sections were then dried at room temperature and stored at -80°C until used.

Fluorescent in situ hybridization:

Fluorescent in situ hybridization was performed with target retrieval, pretreatment, hybridization, amplification, and detection according to the RNAscope Multiplex Fluorescent Reagent Kit v2 Assay User Manual for Fixed Frozen Tissue (ACD). Multiplexed FISH probes for *Pdgrfa* (480661-C2), *Itpr2* (579391-C3) and *Ctps* (1149611-C4) and *Hapln2* (1149621-C1) were used as marker gene probes to identify OPCs, NFOLs, MFOLs, and MOLs, respectively. Slides were cover slipped with Prolong Gold Antifade Mountant with DAPI (Invitrogen, Cat. P36931). Once dried, slides were kept at 4°C until imaged.

Fluorescent in situ hybridization analysis:

Images were first tiled and then max intensity projected. First, a region of interest was drawn around the corpus callosum. Cell ROIs within the corpus callosum were then generated from the DAPI channel using a custom macro program on FIJI. In short, the macro program consisted of auto thresholding the image, converting the image to a mask, applying Gaussian blur (sigma = 3), binarizing the image, inverting the image, applying Watershed, and dilating particles by 1um. Finally, only nuclei between 50-

310µm^2 and a circularity of 0.5-1.0 were selected for analysis. *Pdgrfa*, *Itpr2*, *Ctps*, and *Hapln2* channels were then each individually thresholded and percent coverage for each probe was measured in each cell ROI. Cells were assigned as OPC, NFOL, MFOL, or MOL according to the marker probe with the highest percent coverage in each cell nucleus. Cells were only counted that had a dominant probe percentage coverage > 4% (minimum marker gene expression).

Immunostaining:

All immunostaining was completed on free-floating sections. Sections were first washed in PBS (0.1M, pH 7.4), 3 times for 5 min. Antigen retrieval was then completed by incubating sections in a sodium citrate buffer (10mM, pH 6.0) with Tween 20 (0.5%) for 20min at 80°C. Sections were then cooled and were incubated in PBS with 0.1% triton-X (PBS-TX) and 10% goat serum for 3 hours to reduce subsequent non-specific anti-body binding. The sections were then incubated in PBS-TX with 5% goat serum containing primary antibodies for $Na_v1.6$ (1:500 dilution, ASC-009, Alamone) were incubated overnight at 4°C. Following primary antibody incubation, sections were washed in PBS-TX (3 x 5min) and incubated in PBS-TX containing secondary goat anti-rabbit (1:500 dilution, Ab150077, AlexaFlour 488 goat anti-rabbit, Abcam). Sections were then washed in PBS-TX (3 x 5min) and counter-stained with DAPI (1:500) in PBS-TX for 10 minutes. Lastly, sections were washed in PBS (3 x 5min), mounted onto Superfrost Plus glass slides (Fisher Scientific), and coverslips applied using the ProLong Gold anti-fade (Invitrogen) mounting medium.

Electron microscopy sample preparation:

Brains were first sectioned coronally on a vibratome at 200µm thickness. Comparable posterior sections (-1.82 to -2.30 from Bregma) were selected for each animal, and sections were washed three times in sodium cacodylate buffer (0.1M). The hemispheres of each section were bisected using a razor blade, and a brain punch (0.50mm, Ted Pella Inc) was used to make a hole dorsal to the corpus callosum. Samples were then fixed in resin, and ultra-thin sagittal sections were obtained along the medial edge of the brain. Ultra-thin sections were stained following a previously established protocol[66]. Sections were then imaged on an FEI Tecnai G2 transmission electron microscope. The hole dorsal to the corpus callosum was used to orient the sample and to help differentiate between dorsal and ventral regions within the corpus callosum. Images of the corpus callosum were taken in the dorsal region of the corpus callosum.

Electron microscopy analysis:

For each animal 1-4 images taken at 9300X magnification (105.3µm^2), ~100-300 axons per image, were analyzed using software for semi-automatic myelin *g*-ratio quantification (Myeltracer[67]). Myelinated axons with residual myelin loops and splitting of myelin were classified as axons with myelin abnormalities. To assess myelin decompaction, 10-15 higher magnification images were taken at 68000X magnification and ~20 axons per animal were analyzed.

Microscopy:

All myelin markers, nodal markers, and fluorescent in situ hybridization images were obtained using a Zeiss LSM 880 confocal microscope. Images of fluoromyelin were obtained at a single optical plane, using a 20x objective with tile scans. Images of fluorescent in situ hybridization (DAPI, *Pdgrfa*, *Itpr2*, *Ctps*, and *Hapln2*) were acquired with at 63x oil objective and were comprised of z-stacks with tile scans. All images were obtained using optimized and identical laser settings for all five channels. Electron microscopy images were taken using a FEI Tecnai G2 transmission electron microscope at 9300X magnification.

Myelin purification:

A myelin-enriched membrane fraction was biochemically purified from mouse brains by sucrose density centrifugation and osmotic shocks as described previously[68,69]. Briefly, flash frozen mouse brains were thawed in 0.32M sucrose supplemented with protease inhibitor cocktail tablets (cOmplete Mini EDTA-free; Roche, Mannheim, Germany). Thawed brains were next manually homogenized using a pestle and 16G/25G needle. Brain homogenate was then layered carefully on top of 0.85M sucrose and centrifuged. Following the first sucrose gradient, the band of myelin-enriched fraction found at the 0.32M/0.85M sucrose interphase was collected and washed with distilled water. Two osmotic shocks using cold water were used to diminish cytoplasm and microsomes, followed by a second sucrose gradient and washing. To delipidate the purified myelin protein samples underwent a series of methanol, chloroform, and distilled water washes.

Liquid-Chromatography-Tandem Mass-Spectrometry (LC-MS/MS):

Myelin protein samples, boiled in SDS sample buffer, were run on 10% SDS/PAGE gel. Proteins were detected with colloidal Coomassie G-250 and digested out of the gel as described previously[70]. Samples were purified by solid phase extraction on C-18 STop And Go Extraction (STAGE) Tips. Samples were

separated using a NanoElute UHPLC system (Bruker Daltonics) with Aurora Series Gen2 (CSI) analytical column (25cm x 75µm 1.6µm FSC C18, with Gen2 nanoZero and CSI fitting; Ion Opticks, Parkville, Victoria, Australia) heated to 50°C (by Column toaster M, Bruker Daltonics) and coupled to timsTOF Pro (Bruker Daltonics) operated in DDA-PASEF mode. In a standard 60 min run, the gradient was from 2% B to 12% B over 30 min, then to 33% B from 30 to 60 min, then to 95% B over 0.5 min, held at 95% B for 7.72 min. Before each run, the analytical column was conditioned with 4 column volumes of buffer A. Where buffer A consisted of 0.1% aqueous formic acid and 0.5 % acetonitrile in water, and buffer B consisted of 0.1% formic acid in 99.4 % acetonitrile. The NanoElute thermostat temperature was set at 7°C. The analysis was performed at 0.3 µL/min flow rate.

The Trapped Ion Mobility – Time of Flight Mass Spectrometer (TimsTOF Pro; Bruker Daltonics, Germany) was set to Parallel Accumulation-Serial Fragmentation (PASEF) scan mode for DDA acquisition scanning 100 – 1700 m/z with 5 PASEF ramps. The capillary voltage was set to 1800V, drying gas to 3L/min, and drying temperature to 180°C. The MS and MS/MS spectra were acquired from m/z 100 – 1700. As for TIMS setting, ion mobility range (1/k0) was set to 0.70 – 1.35 V·s/cm^2, 100ms ramp time and accumulation time (100% duty cycle), and ramp rate of 9.42Hz; this resulted in 0.64s of total cycle time.

Linear precursor repetitions were applied with a target intensity of 21,000 and 2500 intensity threshold. The active exclusion was enabled with a 0.4 min release. The collision energy was ramped linearly as a function of mobility from 27eV at 1/k0 = 0.7 V·s/cm^2 to 55eV at 1/k0 = 1.35 V·s/cm^2. Isolation widths were set at 2.07 m/z at < 400 m/z and 3.46 m/z at > 1000 m/z.
Mass accuracy: error of mass measurement is typically within 3 ppm and is not allowed to exceed 7 ppm. For calibration of ion mobility dimension, the ions of Agilent ESI-Low Tuning Mix ions were selected (m/z [Th], 1/k0 [Th]: 622.0290, 0.9915; 922.0098, 1.1986; 1221.9906, 1.3934).

TimsTOF Pro was run with timsControl v. 3.0.0 (Bruker). LC and MS were controlled with HyStar 6.0 (6.0.30.0, Bruker).

Protein Search and Analysis:

Data was analyzed with Fragpipe V18.0, MSFragger V3.5, Philosopher V4.4.0 [71] and quantitation performed using the MaxLFQ algorithm with match between runs enabled (Collins, Woodley, & Choudhary, 2017; Meier, Geyer, Virreira Winter, Cox, & Mann, 2018). The searches were matched to a

mus musculus database downloaded from uniprot.org (reviewed sequences; RRID:SCR_002380) and a contaminant and decoy database. Default search parameters were used except for the following: 50 ppm mass tolerances were used for each of the MS and MS/MS, and MSMS not required for LFQ. Accurately identified peptides were only confined to those with IonScores higher than 99% confidence. Contaminant and reverse hits were removed.

In LFQ, the intensities of the thus recorded peaks are taken as proxies for peptide abundance. With fragmentation spectra (MS2 spectra) used for peptide identification. In LFQ, each sample was separately analyzed on the mass spectrometer, and differential expression was obtained by comparing relative intensities between runs for the same identified peptide (Goeminne, Gevaert, & Clement, 2018). Log ratios were calculated as the difference in average $\log_2$ LFQ intensity values between control and *Zdhhc9*-KO groups.

Statistical analyses:

Prior to analysis, normality and homogeneity of variance were tested for. All values in graphs report the mean ± standard error of the mean. Fluoromyelin staining, FISH, TEM, nodal staining, and proteomics data was analyzed with unpaired two-tailed Student's t test t-tests ($p < 0.05$). TEM axon size and g-ratio distribution analyses were completed using the Kolmogorov–Smirnov test. All major statistical analyses, outlier analyses and graph generation were conducted using GraphPad Prism (Version 8.4.3) software (GraphPad, CA, United States). Asterisks and hashtags are used to denote levels of statistical significance within all graphs (*$p < 0.05$; **$p<0.01$; ***$p<0.001$).

Data availability:

All of the raw and processed high-throughput sequencing data generated in this study have been deposited in the Gene Expression Omnibus database under accession number GSE236665. Raw mass spectrometry data has been deposited in the MassIVE proteomics repository (MSV000092318). All other data generated in this study are available upon reasonable request. Requests for materials and manuscript correspondence should be directed to the corresponding author.

REFERENCES

1. Raymond, F. L. *et al.* Mutations in ZDHHC9, Which Encodes a Palmitoyltransferase of NRAS and HRAS, Cause X-Linked Mental Retardation Associated with a Marfanoid Habitus. *Am. J. Hum. Genet.* **80**, 982–987 (2007).
2. Tzschach, A. *et al.* Next-generation sequencing in X-linked intellectual disability. *Eur. J. Hum. Genet.* **23**, 1513–1518 (2015).
3. Baker, K. *et al.* Epilepsy, cognitive deficits and neuroanatomy in males with ZDHHC9 mutations. *Ann. Clin. Transl. Neurol.* **2**, 559–569 (2015).
4. Masurel-Paulet, A. *et al.* Expanding the clinical phenotype of patients with a *ZDHHC9* mutation. *Am. J. Med. Genet. A.* **164**, 789–795 (2014).
5. Schirwani, S., Wakeling, E., Smith, K., DDD Study & Balasubramanian, M. Expanding the molecular basis and phenotypic spectrum of *ZDHHC9* -associated X-linked intellectual disability. *Am. J. Med. Genet. A.* **176**, 1238–1244 (2018).
6. Boone, P. M. *et al.* Detection of clinically relevant exonic copy-number changes by array CGH. *Hum. Mutat.* **31**, 1326–1342 (2010).
7. Chamberlain, L. H. & Shipston, M. J. The Physiology of Protein *S*- acylation. *Physiol. Rev.* **95**, 341–376 (2015).
8. Han, J. Y. *et al.* The first patient with sporadic X-linked intellectual disability with de novo ZDHHC9 mutation identified by targeted next-generation sequencing. *Eur. J. Med. Genet.* **60**, 499–503 (2017).
9. Grozeva, D. *et al.* Targeted Next-Generation Sequencing Analysis of 1,000 Individuals with Intellectual Disability. *Hum. Mutat.* **36**, 1197–1204 (2015).
10. Han, J. Y., Jang, J. H., Park, J. & Lee, I. G. Targeted Next-Generation Sequencing of Korean Patients With Developmental Delay and/or Intellectual Disability. *Front. Pediatr.* **6**, 391 (2018).
11. Kouskou, M. *et al.* Disruption of the Zdhhc9 intellectual disability gene leads to behavioural abnormalities in a mouse model. *Exp. Neurol.* **308**, 35–46 (2018).
12. Shimell, J. J. *et al.* The X-Linked Intellectual Disability Gene Zdhhc9 Is Essential for Dendrite Outgrowth and Inhibitory Synapse Formation. *Cell Rep.* **29**, 2422-2437.e8 (2019).
13. Bathelt, J., Astle, D., Barnes, J., Raymond, F. L. & Baker, K. Structural brain abnormalities in a single gene disorder associated with epilepsy, language impairment and intellectual disability. *NeuroImage Clin.* **12**, 655–665 (2016).
14. Wild, A. R. *et al.* Exploring the expression patterns of palmitoylating and de-palmitoylating enzymes in the mouse brain using the curated RNA-seq database BrainPalmSeq. *eLife* **11**, e75804 (2022).
15. Marques, S. *et al.* Oligodendrocyte heterogeneity in the mouse juvenile and adult central nervous system. *Science* **352**, 1326–1329 (2016).
16. Sturrock, R. R. MYELINATION OF THE MOUSE CORPUS CALLOSUM. *Neuropathol. Appl. Neurobiol.* **6**, 415–420 (1980).
17. Ku, R. & Torii, M. New Molecular Players in the Development of Callosal Projections. *Cells* **10**, 29 (2020).
18. Sjöstedt, E. *et al.* An atlas of the protein-coding genes in the human, pig, and mouse brain. *Science* **367**, eaay5947 (2020).
19. Jew, B. *et al.* Accurate estimation of cell composition in bulk expression through robust integration of single-cell information. *Nat. Commun.* **11**, 1971 (2020).
20. Wang, X., Park, J., Susztak, K., Zhang, N. R. & Li, M. Bulk tissue cell type deconvolution with multi-subject single-cell expression reference. *Nat. Commun.* **10**, 380 (2019).
21. Kvilekval, K., Fedorov, D., Obara, B., Singh, A. & Manjunath, B. S. Bisque: a platform for bioimage analysis and management. *Bioinformatics* **26**, 544–552 (2010).

22. Hughes, E. G. & Stockton, M. E. Premyelinating Oligodendrocytes: Mechanisms Underlying Cell Survival and Integration. *Front. Cell Dev. Biol.* **9**, 714169 (2021).
23. Zeisel, A. *et al.* Molecular Architecture of the Mouse Nervous System. *Cell* **174**, 999-1014.e22 (2018).
24. Hagemeyer, N. *et al.* Microglia contribute to normal myelinogenesis and to oligodendrocyte progenitor maintenance during adulthood. *Acta Neuropathol. (Berl.)* **134**, 441–458 (2017).
25. Wlodarczyk, A. *et al.* A novel microglial subset plays a key role in myelinogenesis in developing brain. *EMBO J.* **36**, 3292–3308 (2017).
26. Noland, C. L. *et al.* Palmitoylation of TEAD Transcription Factors Is Required for Their Stability and Function in Hippo Pathway Signaling. *Structure* **24**, 179–186 (2016).
27. La Rosa, P., Pesiri, V., Leclercq, G., Marino, M. & Acconcia, F. Palmitoylation Regulates 17β-Estradiol-Induced Estrogen Receptor-α Degradation and Transcriptional Activity. *Mol. Endocrinol.* **26**, 762–774 (2012).
28. Duan, M. *et al.* A Lipid-Anchored NAC Transcription Factor Is Translocated into the Nucleus and Activates *Glyoxalase I* Expression during Drought Stress. *Plant Cell* **29**, 1748–1772 (2017).
29. Eisenhaber, B. *et al.* Nuclear import of a lipid-modified transcription factor: Mobilization of NFAT5 isoform a by osmotic stress. *Cell Cycle* **10**, 3897–3911 (2011).
30. Chen, X. *et al.* EZH2 Palmitoylation Mediated by ZDHHC5 in p53-Mutant Glioma Drives Malignant Development and Progression. *Cancer Res.* **77**, 4998–5010 (2017).
31. Chen, X. *et al.* 2-Bromopalmitate modulates neuronal differentiation through the regulation of histone acetylation. *Stem Cell Res.* **12**, 481–491 (2014).
32. Chen, X. *et al.* Protein Palmitoylation Regulates Neural Stem Cell Differentiation by Modulation of EID1 Activity. *Mol. Neurobiol.* **53**, 5722–5736 (2016).
33. Zou, C. *et al.* Acyl-CoA:Lysophosphatidylcholine Acyltransferase I (Lpcat1) Catalyzes Histone Protein O-Palmitoylation to Regulate mRNA Synthesis. *J. Biol. Chem.* **286**, 28019–28025 (2011).
34. Wilson, J. P., Raghavan, A. S., Yang, Y.-Y., Charron, G. & Hang, H. C. Proteomic Analysis of Fatty-acylated Proteins in Mammalian Cells with Chemical Reporters Reveals S-Acylation of Histone H3 Variants. *Mol. Cell. Proteomics* **10**, M110.001198 (2011).
35. Gong, Y. *et al.* Sterol-regulated ubiquitination and degradation of Insig-1 creates a convergent mechanism for feedback control of cholesterol synthesis and uptake. *Cell Metab.* **3**, 15–24 (2006).
36. Eberlé, D., Hegarty, B., Bossard, P., Ferré, P. & Foufelle, F. SREBP transcription factors: master regulators of lipid homeostasis. *Biochimie* **86**, 839–848 (2004).
37. Saher, G. & Stumpf, S. K. Cholesterol in myelin biogenesis and hypomyelinating disorders. *Biochim. Biophys. Acta BBA - Mol. Cell Biol. Lipids* **1851**, 1083–1094 (2015).
38. Saher, G. *et al.* High cholesterol level is essential for myelin membrane growth. *Nat. Neurosci.* **8**, 468–475 (2005).
39. Mathews, E. S. & Appel, B. Cholesterol Biosynthesis Supports Myelin Gene Expression and Axon Ensheathment through Modulation of P13K/Akt/mTor Signaling. *J. Neurosci.* **36**, 7628–7639 (2016).
40. Saher, G., Quintes, S. & Nave, K.-A. Cholesterol: A Novel Regulatory Role in Myelin Formation. *The Neuroscientist* **17**, 79–93 (2011).
41. Montani, L. Lipids in regulating oligodendrocyte structure and function. *Semin. Cell Dev. Biol.* **112**, 114–122 (2021).
42. Ito, M. *et al.* Age-dependent decline in remyelination capacity is mediated by apelin–APJ signaling. *Nat. Aging* **1**, 284–294 (2021).
43. Chavali, M. *et al.* Wnt-Dependent Oligodendroglial-Endothelial Interactions Regulate White Matter Vascularization and Attenuate Injury. *Neuron* **108**, 1130-1145.e5 (2020).
44. Shin, D., Howng, S. Y. B., Ptáček, L. J. & Fu, Y.-H. miR-32 and its target SLC45A3 regulate the lipid metabolism of oligodendrocytes and myelin. *Neuroscience* **213**, 29–37 (2012).

45. Jouaud, M. *et al.* Rodent models with expression of PMP22: Relevance to dysmyelinating CMT and HNPP. *J. Neurol. Sci.* **398**, 79–90 (2019).
46. Bull, S.-J. *et al.* Progressive Disorganization of Paranodal Junctions and Compact Myelin Due to Loss of DCC Expression by Oligodendrocytes. *J. Neurosci.* **34**, 9768–9778 (2014).
47. García-Mateo, N. *et al.* Myelin extracellular leaflet compaction requires apolipoprotein D membrane management to optimize lysosomal-dependent recycling and glycocalyx removal. *Glia* **66**, 670–687 (2018).
48. Grandis, M. *et al.* ALTERED DOSAGE OF PERIPHERAL MYELIN PROTEIN 22 (PMP22) AFFECTS MYELIN PERIODICITY. *J. Peripher. Nerv. Syst.* **5**, 41–41 (2000).
49. Griffiths, I. R., Duncan, I. D. & McCulloch, M. Shaking pups: a disorder of central myelination in the spaniel dog. II. Ultrastructural observations on the white matter of the cervical spinal cord. *J. Neurocytol.* **10**, 847–858 (1981).
50. Myelin abnormalities in mice deficient in galactocerebroside and sulfatide.
51. Focke, N. K. *et al.* Idiopathic-generalized epilepsy shows profound white matter diffusion-tensor imaging alterations: Diffusion Tensor Alterations in Generalized Epilepsy. *Hum. Brain Mapp.* **35**, 3332–3342 (2014).
52. Hutchinson, E. *et al.* Children with new-onset epilepsy exhibit diffusion abnormalities in cerebral white matter in the absence of volumetric differences. *Epilepsy Res.* **88**, 208–214 (2010).
53. Chahboune, H. *et al.* DTI abnormalities in anterior corpus callosum of rats with spike–wave epilepsy. *NeuroImage* **47**, 459–466 (2009).
54. Sharma, P. *et al.* Differences in white matter structure between seizure prone (FAST) and seizure resistant (SLOW) rat strains. *Neurobiol. Dis.* **104**, 33–40 (2017).
55. Riedhammer, K. M. *et al. De novo* stop-loss variants in *CLDN11* cause hypomyelinating leukodystrophy. *Brain* **144**, 411–419 (2021).
56. Yoshikawa, H. Myelin-associated oligodendrocytic basic protein modulates the arrangement of radial growth of the axon and the radial component of myelin. *Med. Electron Microsc.* **34**, 160–164 (2001).
57. Beirowski, B. *et al.* Sir-two-homolog 2 (Sirt2) modulates peripheral myelination through polarity protein Par-3/atypical protein kinase C (aPKC) signaling. *Proc. Natl. Acad. Sci.* **108**, (2011).
58. Werner, H. B. *et al.* Proteolipid Protein Is Required for Transport of Sirtuin 2 into CNS Myelin. *J. Neurosci.* **27**, 7717–7730 (2007).
59. Quarles, R. H. Myelin-associated glycoprotein (MAG): past, present and beyond. *J. Neurochem.* **0**, 070214184024009-??? (2007).
60. Schneider, A. *et al.* Palmitoylation is a sorting determinant for transport to the myelin membrane. *J. Cell Sci.* **118**, 2415–2423 (2005).
61. Franklin, K. B. J. & Paxinos, G. *The mouse brain in stereotaxic coordinates*. (Elsevier, AP, 2008).
62. Bray, N. L., Pimentel, H., Melsted, P. & Pachter, L. Near-optimal probabilistic RNA-seq quantification. *Nat. Biotechnol.* **34**, 525–527 (2016).
63. Love, M. I., Huber, W. & Anders, S. Moderated estimation of fold change and dispersion for RNA-seq data with DESeq2. *Genome Biol.* **15**, 550 (2014).
64. Szklarczyk, D. *et al.* STRING v11: protein–protein association networks with increased coverage, supporting functional discovery in genome-wide experimental datasets. *Nucleic Acids Res.* **47**, D607–D613 (2019).
65. Baldarelli, R. M. *et al.* The mouse Gene Expression Database (GXD): 2021 update. *Nucleic Acids Res.* **49**, D924–D931 (2021).
66. Ghnenis, A. B., Czaikowski, R. E., Zhang, Z. J. & Bushman, J. S. Toluidine Blue Staining of Resin-Embedded Sections for Evaluation of Peripheral Nerve Morphology. *J. Vis. Exp.* 58031 (2018) doi:10.3791/58031.

67. Kaiser, T. *et al.* MyelTracer: A Semi-Automated Software for Myelin *g* -Ratio Quantification. *eneuro* **8**, ENEURO.0558-20.2021 (2021).
68. Erwig, M. S., Kusch, K., Tenzer, S., Jahn, O. & Werner, H. B. Myelin: Methods for Purification and Proteome Analysis. 27.
69. Jahn, O. *et al.* The CNS Myelin Proteome: Deep Profile and Persistence After Post-mortem Delay. *Front. Cell. Neurosci.* **14**, 239 (2020).
70. Chan, Q. W. T., Howes, C. G. & Foster, L. J. Quantitative Comparison of Caste Differences in Honeybee Hemolymph. *Mol. Cell. Proteomics* **5**, 2252–2262 (2006).
71. Kong, A. T., Leprevost, F. V., Avtonomov, D. M., Mellacheruvu, D. & Nesvizhskii, A. I. MSFragger: ultrafast and comprehensive peptide identification in mass spectrometry–based proteomics. *Nat. Methods* **14**, 513–520 (2017).

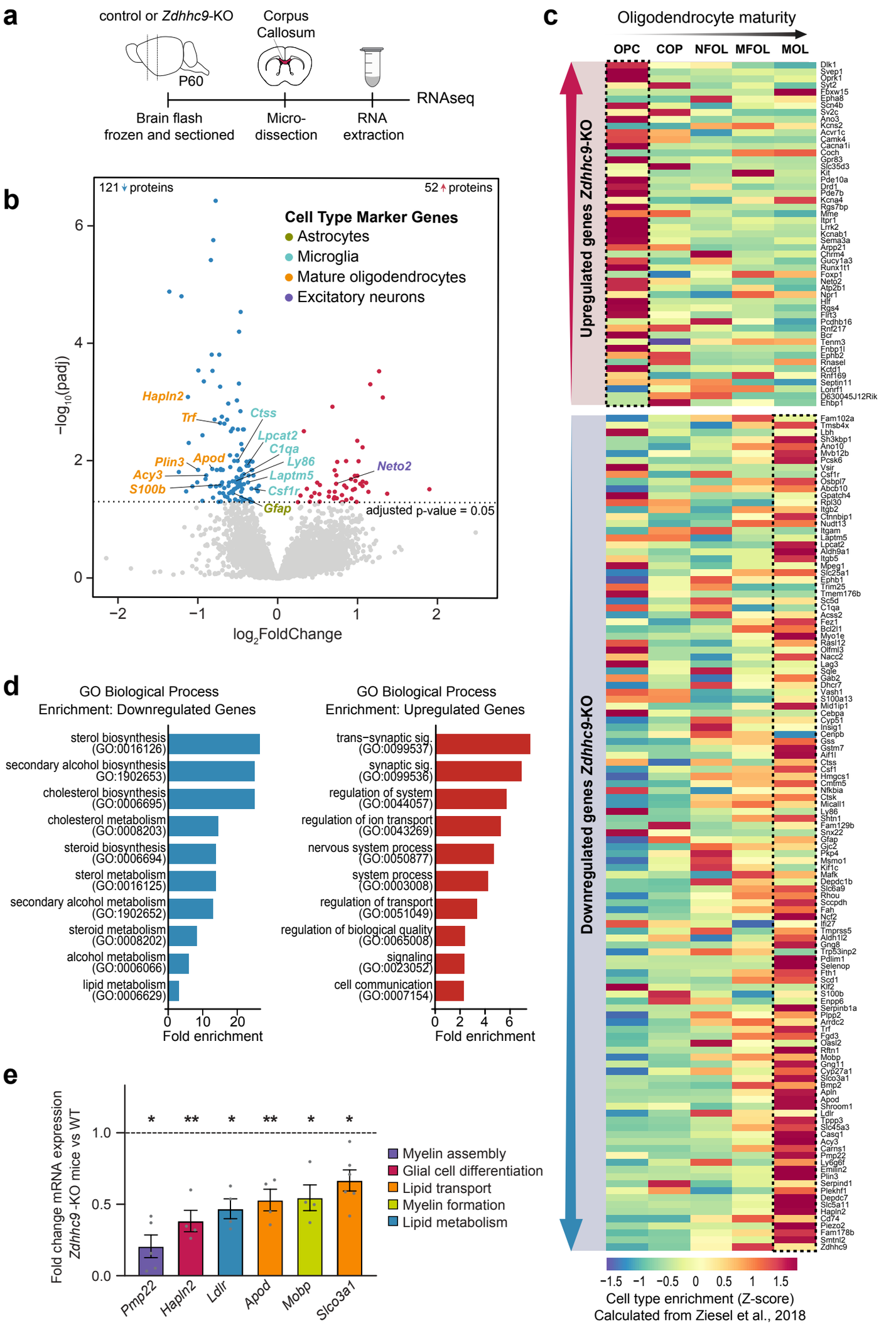

Figure 1: There is a decrease in MOL marker gene expression and genes involved in lipid metabolism in the corpus callosum of *Zdhhc9*-KO mice

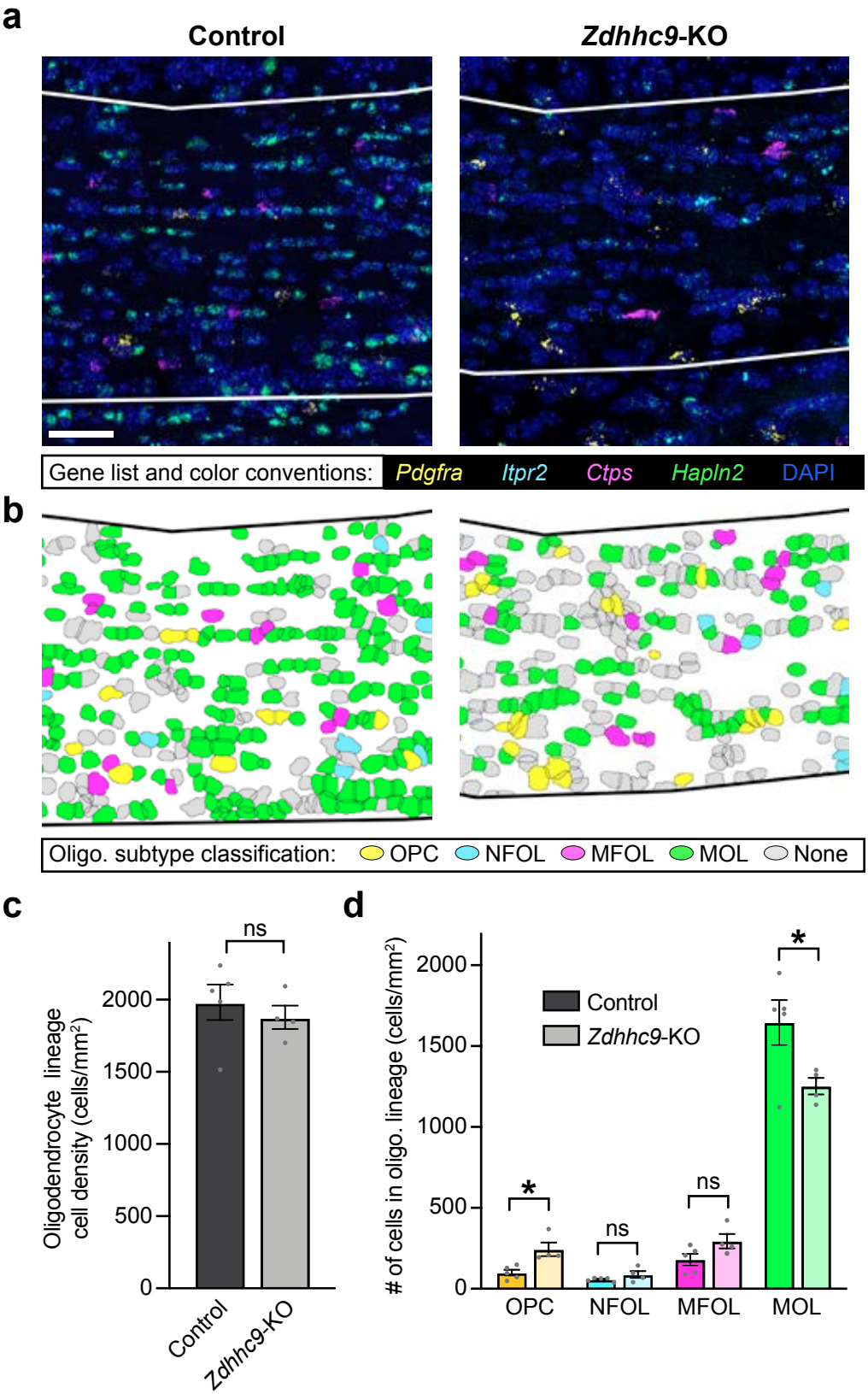

Figure 2: There is a decrease in the density of MOLs and an increase in the density of OPCs in the corpus callosum of *Zdhhc9*-KO mice

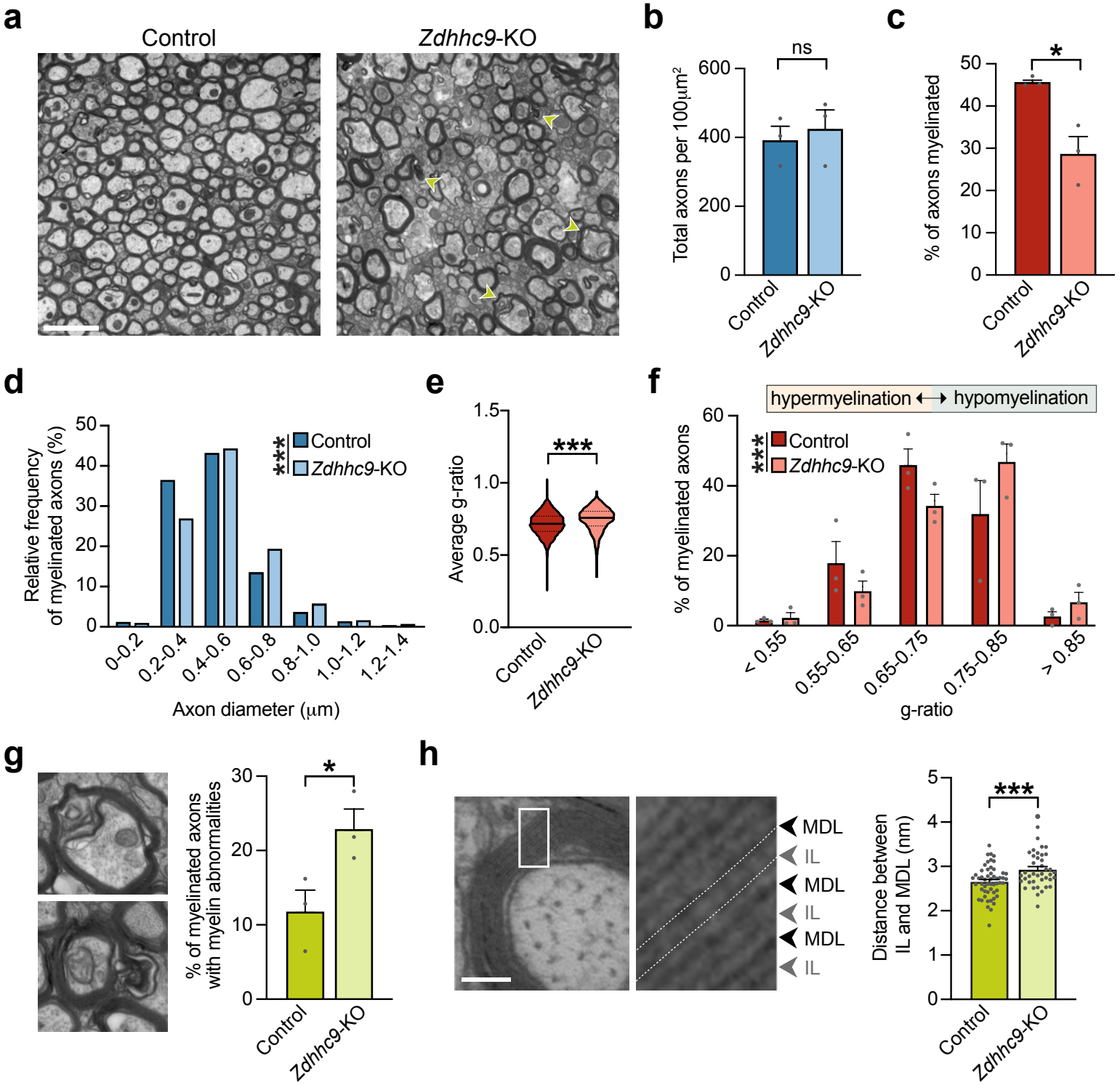

Figure 3: There are fewer myelinated axons and increased myelin decompaction in the corpus callosum of *Zdhhc9*-KO mice

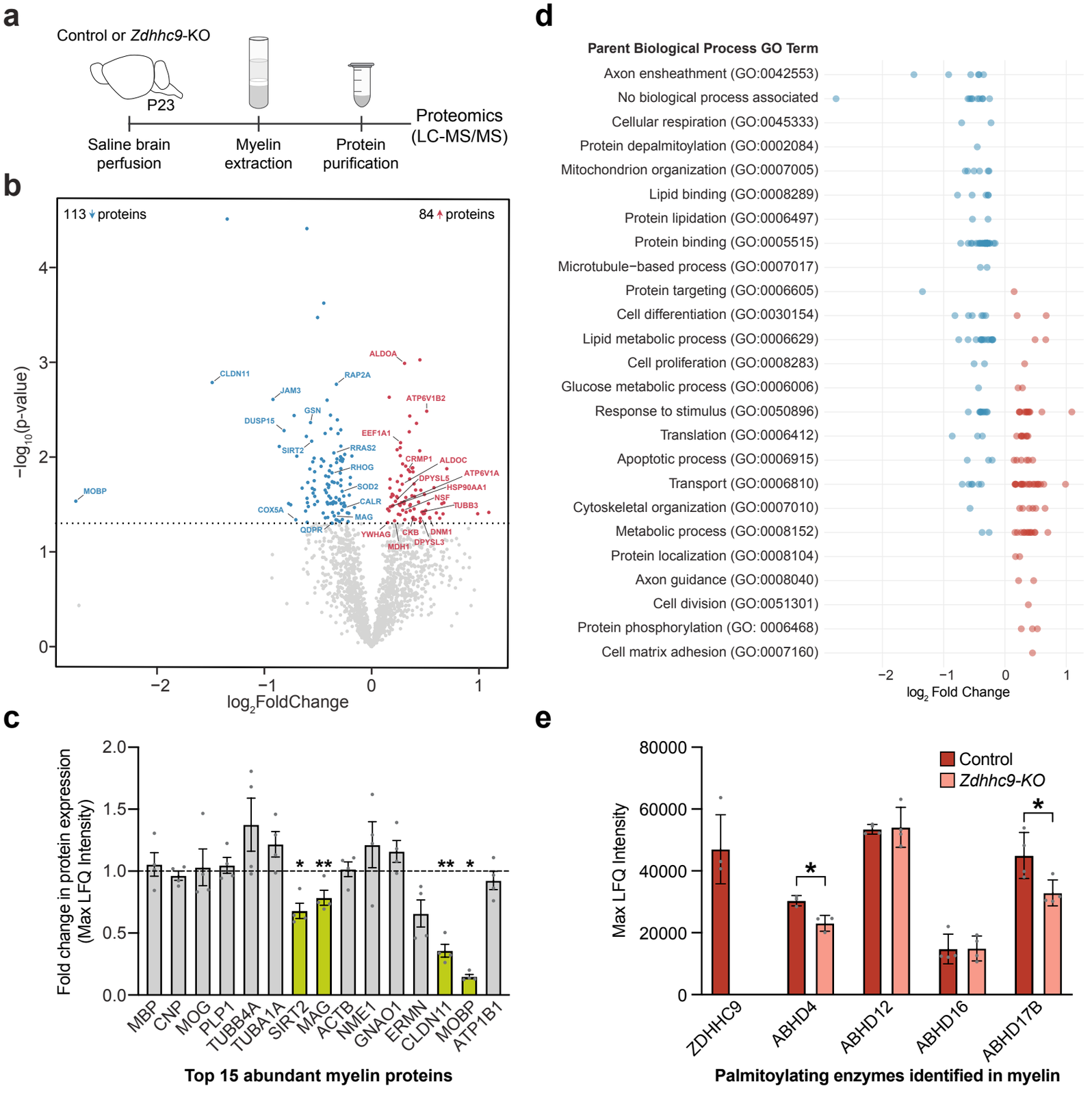

Figure 4: Proteins associated with myelination and myelin compaction are decreased in *Zdhhc9*-KO mice

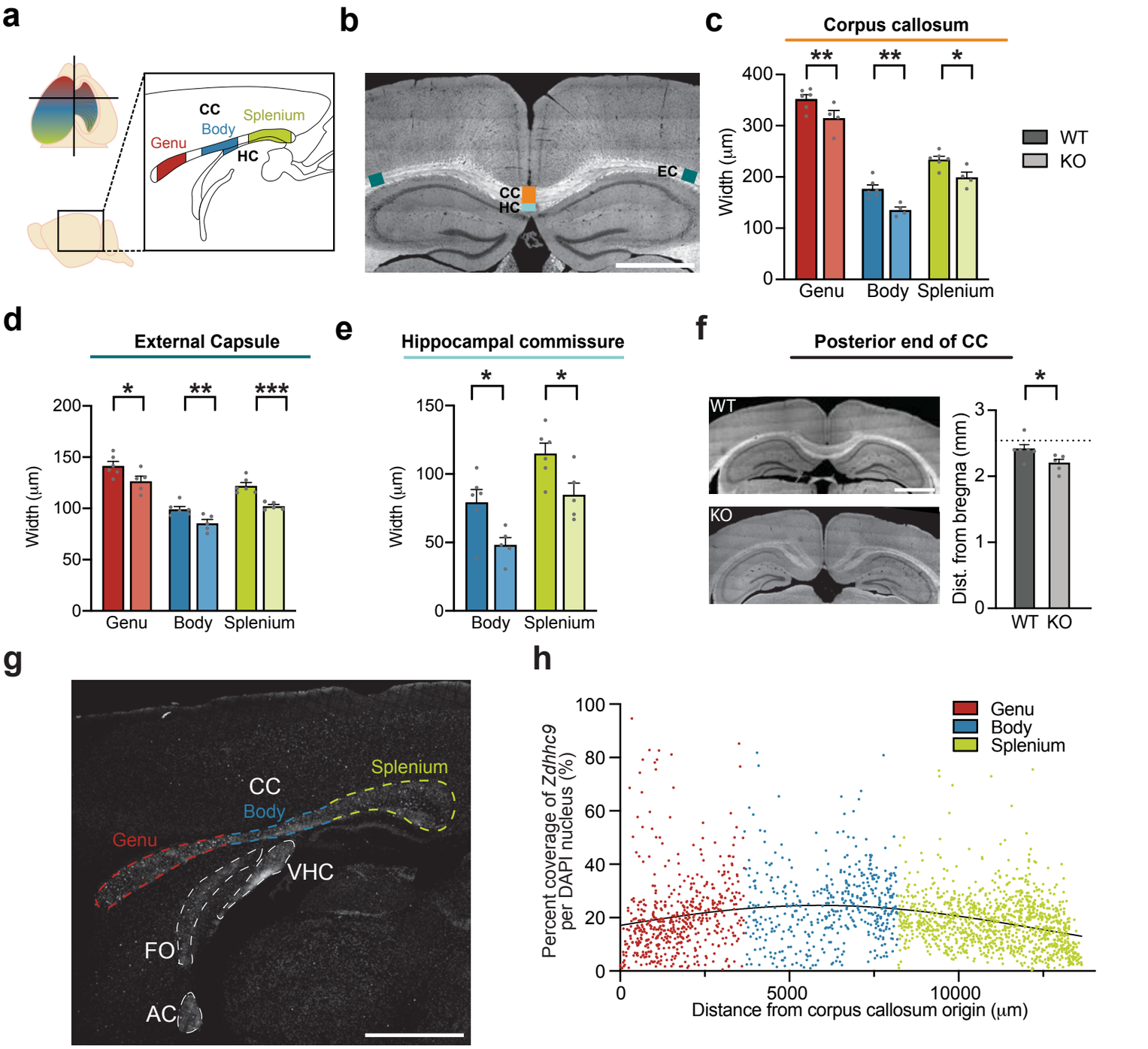

Figure S1: There is a uniform reduction in white matter tracts in *Zdhhc9*-KO mice and a uniform expression of *Zdhhc9* throughout the anterior posterior axis of the corpus callosum

a, (Top left) Schematic of the brain (horizontal plane), illustrating the spatial relationship between the position of cortical regions and the respective location their projections cross the anterior posterior axis of the corpus callosum. (Right) Schematic of the anterior-posterior axis of the corpus callosum, colored based on its main anatomical subdivisions: genu (red), body (blue), splenium (green). The location of these colored regions indicates where measurements were taken for subsequent morphological analyses. **b,** Representative image illustrating white matter tracts that were quantified (corpus callosum, hippocampal commissure, external capsule), and the relative position where measurements were taken within each tract (scale bar, 1mm). **c,** Width of the corpus callosum (n = 4 *Zdhhc9*-KO, n = 6 control) **d,** the external capsule and **e,** the hippocampal commissure in control and *Zdhhc9*-KO mice. (n = 5 *Zdhhc9*-KO, n = 6 control) **f,** Representative images of the posterior location at which the corpus callosum terminates in control and *Zdhhc9*-KO mice (scale bar, 1mm). Distance from bregma at which the corpus callosum terminates in control and *Zdhhc9*-KO mice. **g,** Representative image of FISH for *Zdhhc9* along the anterior-posterior axis of the corpus callosum (scale bar, 1mm). White matter tracts are labeled with dashed lines, along with the main subdivisions of the corpus callosum (colored as in **a,**). **h,** Percent coverage of *Zdhhc9* labeling per cell as a function of distance from the origin of the corpus callosum. Points are colored based on sub-regions delineated in **h,** (n of at least 500 cells per region from 1 animal). Data in **c, d, e, f,** represent mean + SEM, all statistical tests were two-tailed unpaired Student's t-tests. CC=corpus callosum, HC=hippocampal commissure, FO=Fornix, VHC=Ventral hippocampal commissure, AC=anterior commissure.

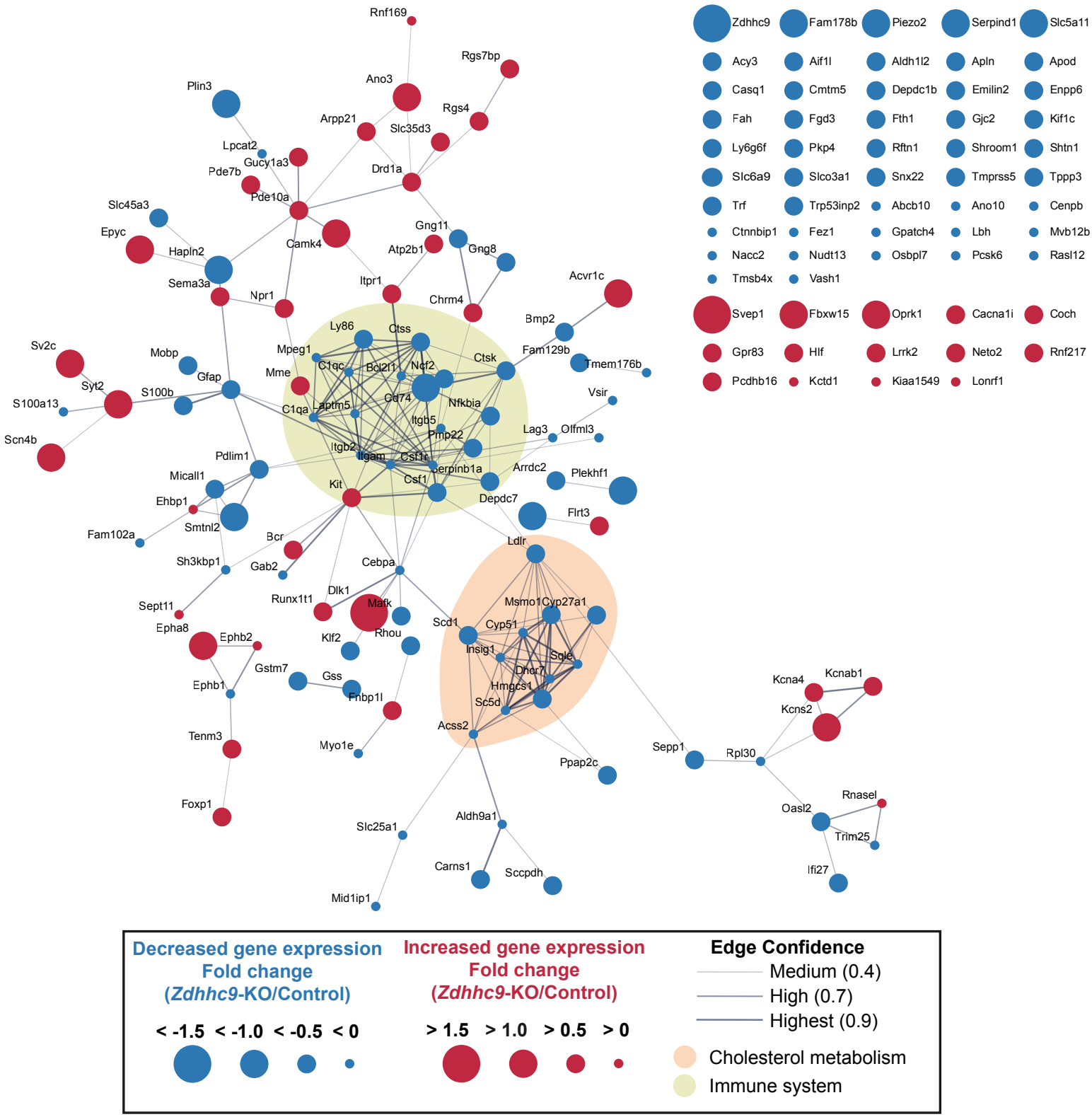

Figure S2: Protein-protein interaction analysis of differentially expressed genes
STRING analysis highlighting protein-protein interactions between differentially expressed genes identified from RNAseq (left). Blue nodes represent downregulated genes, red nodes represent upregulated genes and the node size depicts the magnitude of the fold change in gene expression. Lines (edges) between nodes show predicted protein-protein interactions, and the corresponding line-width reflects the confidence of protein-protein interactions. Two groups of proteins with high densities of interactions were noted and contain proteins with known roles in cholesterol metabolism (orange circle) and immune system function (green circle). Differentially expressed genes without predicted protein-protein interactions are also shown (right).

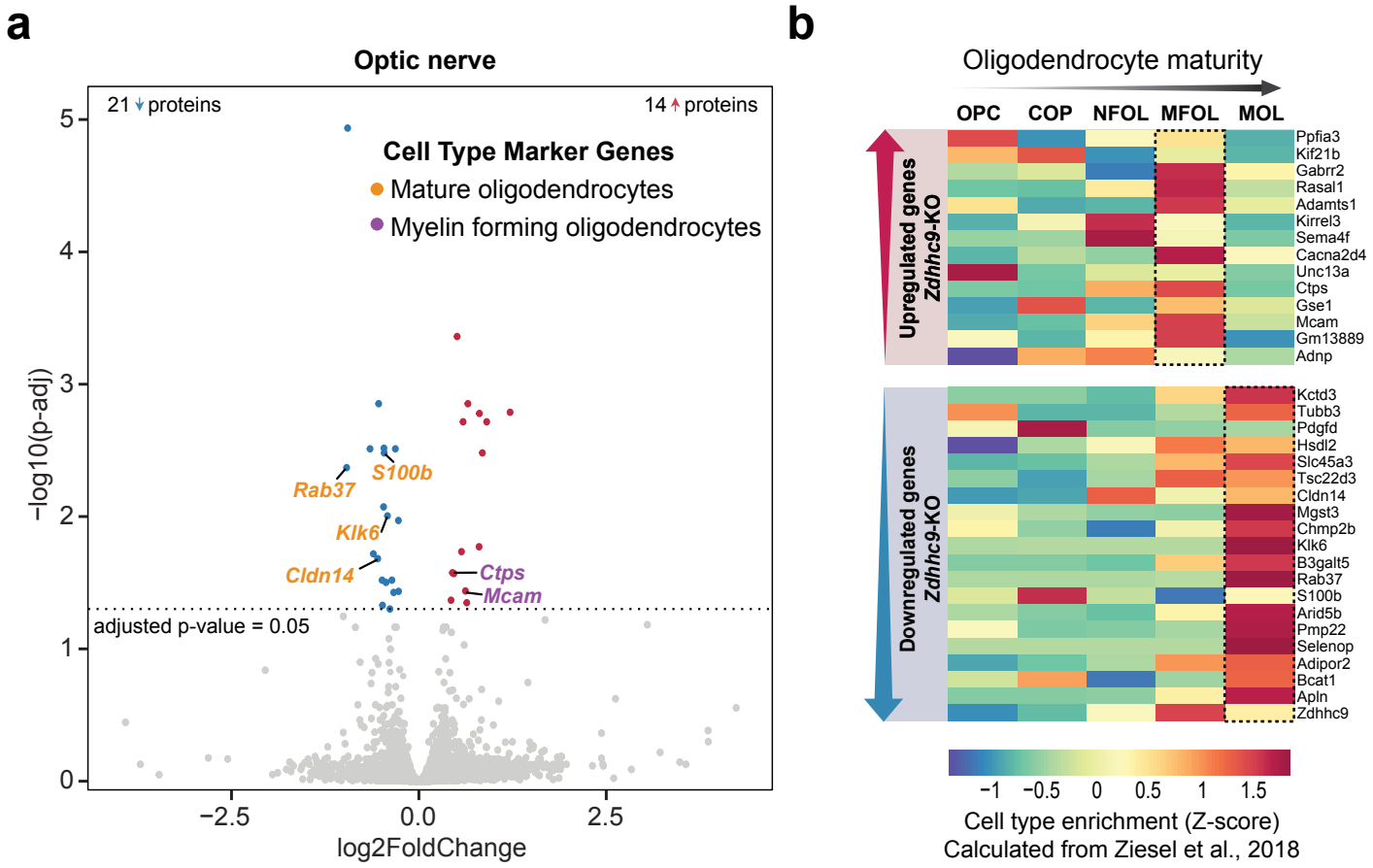

Figure S3: There is a change in gene expression in the optic nerve of *Zdhhc9*-KO mice

a, Quantification of fold change in gene expression in *Zdhhc9*-KO optic nerve compared to control mice (*n* = 5 *Zdhhc9*-KO, *n* = 4 control). Each point represents an individual gene; blue denotes genes that are downregulated, and red denotes genes that are upregulated in *Zdhhc9*-KO mice relative to controls. The horizontal line denotes the statistical significance threshold required for two tailed t-tests; p-values were adjusted to account for multiple comparisons. Differentially expressed cell type marker genes are labelled. **b,** Heatmaps showing the expression of the 35 differentially expressed genes within different oligodendrocyte subtypes using single-cell RNAseq data from Mousebrain. Genes are listed (top to bottom) by decreasing $\log_2$ Fold Change (i.e. from most upregulated to the most downregulated). Dotted black boxes highlight overall enrichment of upregulated and downregulated genes.

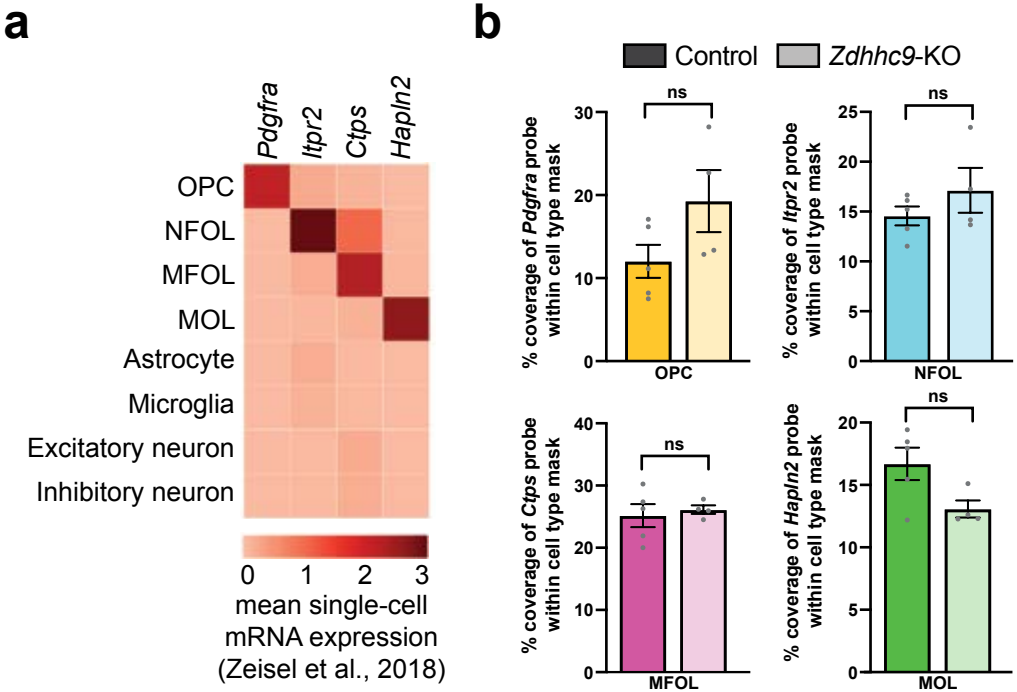

Figure S4: Overall levels of oligodendrocyte lineage marker gene expression does not differ between *Zdhhc9*-KO and control mice.

a, Heatmap of gene expression for our oligodendrocyte lineage marker genes, across different cell types and maturation stages within the oligodendrocyte lineage (single-cell RNAseq from Mousebrain). **b,** Graphs depicting the average coverage of oligodendrocyte lineage probes per cell (n = 4 mice per genotype). Data shows mean + SEM, and statistical analyses were done using unpaired two-tailed Student's t-tests.

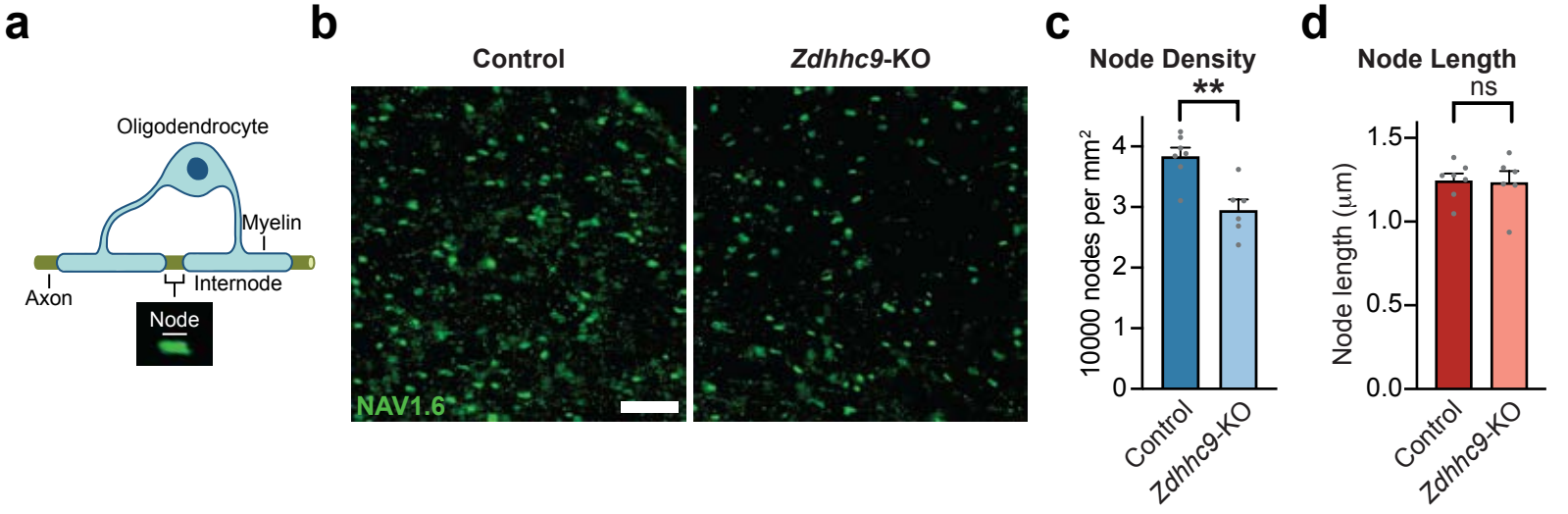

Figure S5: There is a reduction in the density of nodes of Ranvier in *Zdhhc9*-KO mice

a, Illustration of a myelinated axon and node of Ranvier. **b,** Representative images of the nodal marker, NAV1.6, within the corpus callosum of *Zdhhc9*-KO and control mice (scale bar, 10μm). **c,** The density of nodes and **d,** the length of nodes in *Zdhhc9*-KO and control mice (n = 6 *Zdhhc9*-KO, n = 7 control). Data in **c,** and **d,** represent mean + SEM, statistical tests were done using unpaired two-tailed Student's t-tests.

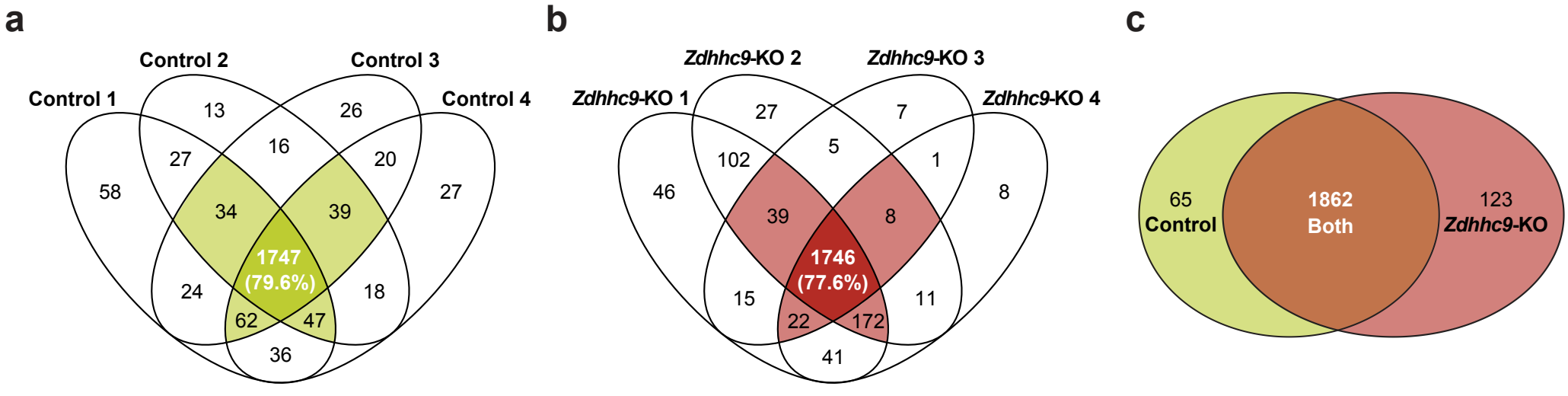

Figure S6: Analysis of proteins identified in both *Zdhhc9*-KO and control myelin samples.

Venn diagrams showing the overlap of proteins identified in **a,** control and **b,** *Zdhhc9*-KO samples. **c,** Venn diagram of myelin proteins identified in at least 3 Zdhhc9-KO and control samples.